ADVANCED FUNCTIONAL MATERIALS
www.afm-journal.de

Eco-Friendly Approach to Ultra-Thin Metal Oxides- Solution Sheared Aluminum Oxide for Half-Volt Operation of Organic Field-Effect Transistors

*Preetam Dacha, Katherina Haase, Angelika Wrzesińska-Lashkova, Darius Pohl, Roman Maletz, Vojtech Millek, Alexander Tahn, Bernd Rellinghaus, Christina Dornack, Yana Vaynzof, Mike Hambsch, and Stefan C. B. Mannsfeld**

Sol–gel-based solution-processed metal oxides have emerged as a key fabrication method for applications in thin film transistors both as a semiconducting and a dielectric layer. Here, a low-temperature, green solvent-based, non-toxic, and cost-effective solution shearing approach for the fabrication of thin aluminum oxide (AlO_x) dielectrics is reported. Optimization of sustainability aspects like energy demand, and selection of chemicals used allows to reduce the environmental impact of the life cycle of the resulting product already in the design phase. Using this approach, ultra-thin, device-grade AlO_x films of 7 nm are coated—the thinnest films to be reported for any solution-fabrication method. The metal oxide formation is achieved by both thermal annealing and deep ultra-violet (UV) light exposure techniques, resulting in capacitances of 750 and 600 nF cm^{-2}, respectively. The structural analysis using microscopy and x-ray spectroscopy techniques confirmed the formation of smooth, ultra-thin AlO_x films. These thin films are employed in organic field-effect transistors (OFETs) resulting in stable, low hysteresis devices leading to high mobilities (6.1 ± 0.9 cm^2 V^{-1} s^{-1}), near zero threshold voltage (−0.14 ± 0.07 V) and a low subthreshold swing (96 ± 16 mV dec^{-1}), enabling device operation at only ±0.5 V with a good I_{on}/I_{off} ratio (3.7×10^5).

1. Introduction

Metal oxides remain the primary choice for solution-processed air-stable n-type semiconductors and dielectric films in electronics due to their ability to be processed at low temperatures with extremely low thicknesses and large-scale fabrication opportunities.[1–4] In addition to the conventional silicon oxide (SiO_2), vacuum-processed aluminum oxide (AlO_x), zirconium oxide, hafnium oxide, and titanium oxide thin films have been utilized as a capacitive material for its high dielectric constant and suitability for the fabrication of low-power electronic devices.[5–9] However, there is also the opportunity to replace the vacuum-based deposition with coating or printing methods that offer attractive benefits of fast and cheap processing of dielectric thin films in the industry for large-area fabrication.[10–14] Besides that, lower energy demands for the process result in a

P. Dacha, K. Haase, V. Millek, M. Hambsch, S. C. B. Mannsfeld
Center for Advancing Electronics Dresden (CFAED)
TUD Dresden University of Technology
01069 Dresden, Germany
E-mail: stefan.mannsfeld@tu-dresden.de

P. Dacha, K. Haase, V. Millek, S. C. B. Mannsfeld
Faculty of Electrical and Computer Engineering
TUD Dresden University of Technology
01069 Dresden, Germany

A. Wrzesińska-Lashkova, Y. Vaynzof
Chair for Emerging Electronic Technologies
TUD Dresden University of Technology
Nöthnitzer Str. 61, 01187 Dresden, Germany

A. Wrzesińska-Lashkova, Y. Vaynzof
Leibniz-Institute for Solid State and Materials Research Dresden
Helmholtzstraße 20, 01069 Dresden, Germany

D. Pohl, A. Tahn, B. Rellinghaus
Dresden Center for Nanoanalysis (DCN)
Center for Advancing Electronics Dresden (cfaed)
TUD Dresden University of Technology
D-01062 Dresden, Germany

R. Maletz, C. Dornack
Institute of Waste Management and Circular Economy
TUD Dresden University of Technology
Pratzschwitzer Str. 15, 01796 Pirna, Germany

The ORCID identification number(s) for the author(s) of this article can be found under https://doi.org/10.1002/adfm.202315850

DOI: 10.1002/adfm.202315850

decreased environmental impact like reduced CO_2-equivalent emissions, which helps to improve making the production of semiconductor devices more sustainable.[15]

High-k Inorganic metal oxides like zirconium oxide and hafnium oxide can result in dielectric thin films with very high capacitance values.[7–9] However, their utility in transistors contributes to undesired effects like polarization due to their inherent ferroelectric behavior.[16] Further, their tendency to crystallize and therefore a higher roughness also hinders the ease of fabrication of semiconductor films on them. An interesting material that underlines the key metrics like high-k, large bandgap, smooth, and amorphous thin film for the fabrication of high capacitance dielectric is aluminum oxide. While early reports demonstrated the fabrication of AlO_x thin films using spin-coating, this process relies on high annealing temperatures (>350 °C) and the use of solvents like 2-methoxy ethanol (2-ME) that are known to be highly toxic. Recent publications focused on the development of methods to minimize the environmental impact of fabrication by the reduction of waste, use of eco-friendly precursors, combustion mechanisms, and a decrease of thermal budget.[2,3,13,17–19] A promising example of such efforts is the utilization of the UV photo-activation of metal oxide precursors.[20–22] John et al. discussed the utilization of the UV process for indium oxide (In_2O_3) and indium zinc oxide (IZO) thin films.[20] Recently, Lee et al. applied this mechanism for AlO_x thin films by employing deep UV photo-activation (DUV, below ≈250 nm).[23] However, the use of 2-ME as the solvent in these reports limits their applicability. As a non-toxic alternative, Branquinho et al. showed the utility of aqueous solutions for the synthesis of metal oxide thin films.[24] All these reports have employed spin-coating as the deposition technique which resulted in rather thick (>20 nm) films. Additionally, this technique involves a higher degree of material waste while processing. Alternatively, reports have also suggested techniques like anodization or plasma oxidation of Al contacts for <10 nm growth of AlO_x films.[11,12,25] However, this process still requires the contact evaporation to be done under high vacuum conditions resulting, in most scenarios, in an energy-intensive process.[26] Recently, Tang et al. published the application of aqueous metal oxide solutions for thin film fabrication via solution shearing, a meniscus-guided coating method.[4] Here, a multi-layer coating of AlO_x thin films was performed and a thermal budget as low as annealing at 300 °C for 5 min per layer coating was proposed. While a new method for fabrication and a low thermal annealing budget were reported, the possibility of an ultra-thin film by deposition of a single layer is yet to be explored.

Eco-friendly here can be understood as considering environmental advantages besides other criteria like performance or functionality improvement, thickness reduction, or lower demand for process chemicals. Implementing such criteria in the design process of a product or process is necessary under today's and expected challenges in mitigating climate change, loss of biodiversity, or depletion of resources. Environmental assessment during semiconductor process development has not been implemented comprehensively yet due to other premises but is useful to compare established and new processing methods by their environmental performance.[27] The energy demand for avoiding vacuum processing and using low temperatures is directly connected to the process of greenhouse gas (GHG) emissions. The cumulative energy demand is one of the main contributors in the overall GHG-emission inventory of the considered process system, it can lead to high reductions of environmental burdens in the life cycle of the resulting product.[28]

Here, we report the fabrication of ultra-thin AlO_x films that combine the benefits of low-temperature, eco-friendly, and UV processing techniques with minimal material use. We report a simple way to solution shear ultra-thin, high-quality AlO_x films from de-ionized (DI) water without the use of any additional fuels and demonstrate their application as a device-grade, high-capacitance dielectric layer. Furthermore, we show that OFETs can be fabricated using these films, resulting in operation at extremely low voltages of −0.5 V, suitable for low-power electronics.

2. Results and Discussion

2.1. Sample Preparation

Aluminum nitrate nonahydrate ($Al(NO_3)_3 \bullet 9H_2O$) salt was considered as the precursor for the metal oxide sol–gel formation in DI-water due to their relatively lower decomposition temperature and better UV absorption over their chloride and acetate counterparts.[20] The procedure used for the solution preparation resembles the one reported in the literature.[4] Briefly, a 0.2 M solution was filtered using a 0.2 µm PTFE filter. A volume of 2.5 µL solution was used to coat a uniform thin film on a 3.5 cm × 1.25 cm Si substrate using an in-house solution shearing setup.[29,30] For all precursor deposition, we used a silicon oxide blade coated with an octadecyltrimethoxysilane self-assembled monolayer at a moving speed of 10 mm s^{-1}. The substrate was maintained at a temperature of 80 °C throughout the coating.

Two annealing techniques, one high (>200 °C) and another low (<150 °C) temperature-based, were utilized here to fabricate the metal oxide network of aluminum oxide. Besides, thermal annealing for the metal oxide network formation from the sol–gel, the utility of DUV photo-activation has also been discussed as a viable alternative. This is because the DUV photo-activation facilitates the subsequent formation of a metal oxide network.[4,20,23,24] This is observed due to the presence of NO and OH radicals, known to widely promote the densification of metal oxide films via DUV light absorption.[21,23] The first process has been chosen from the optimized thermal budget of 300 °C for 5 min (hereby termed Th) as previously reported.[4] Additionally, the low-temperature annealing process utilizing the DUV photo-activation has also been employed. For the AlO_x thin film fabrication using the DUV-exposure technique, the as-coated sample was exposed to a soft bake of 120 °C for 2 min followed by a varied exposure duration (1–20 min) of DUV photo-activation. The soft bake was implemented to remove any traces of DI water in the thin film.[1] DUV photo-activation was carried out under a UV lamp setup (emission wavelengths of 185 and 254 nm), estimated to produce an irradiance of ≈18 mW cm^{-2}. This DUV source ensures that the chemical transformation can be triggered easily due to its capability to decompose the bonds in our precursor system.[20,23] Additionally, the possibility of ozone release during exposure can aid the condensation and densification of the metal oxide network due to the formation of unstable oxygen radicals.[20,31] A schematic of the procedure is depicted in **Figure 1**. The ultra-thin films coated using solution shearing

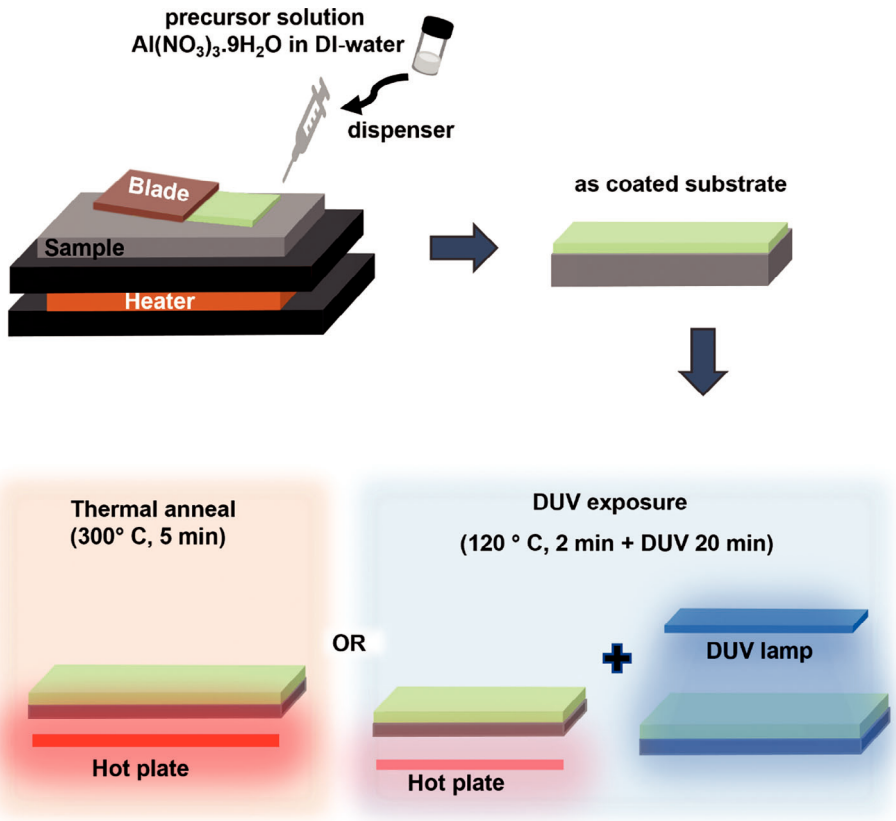

Figure 1. Schematic diagram of the solution shearing and annealing techniques used in this research to fabricate ultra-thin AlO_x films for low-voltage device applications.

(7 nm) provide the foundation for DUV penetration and activation of the film resulting in oxide formation.

2.2. Thin Film Characteristics

To analyze the metal oxide network formation in the Th-annealed and DUV-exposed samples, X-ray photoemission spectroscopy (XPS) measurements were performed. The survey spectra of the samples treated for different Th-annealing and DUV-exposure durations are shown in Figure S1 (Supporting Information). The elemental composition has been evaluated from the XPS spectra as shown in Table S1 (Supporting Information) showing the presence of carbon in the films. This is attributed to the sample's exposure to ambient conditions prior to XPS measurements.[12,32,33] The charging effect in all the samples was adjusted by considering this carbon (C1s) peak at a binding energy of 284.8 eV as a reference value.[33] Furthermore, a negligible percentage of nitrogen was observed in the samples which can be attributed to traces from the precursor solution.[3] The major peaks obtained in the survey scan for these films were at the binding energy values of ≈75 and 532 eV, which are the relative positions of the Al2p and O1s peaks, respectively.[12,18,34] In order to further evaluate the chemical composition of the aluminum and oxygen in the samples, high-resolution spectra in the binding energy range of Al2p and O1s peak regions were performed. The Al2p spectra are shown in Figure S2 (Supporting Information). For the Th-annealed samples, the single Al2p doublet at a binding energy of 74.2 ± 0.3 eV is consistent with a metal oxide network formation as reported in the literature.[3,4]

Interestingly, the Al2p peak at 75 eV for the soft-bake sample was observed to shift toward lower binding energy values with an increase in the DUV-exposure time. This shift toward the lower binding energy is attributed to the decrease of OH^- concentration which can also be observed from the atomic percentages of the survey spectra as discussed earlier in Table S1 (Supporting Information).[3] Interestingly, beyond the DUV exposure of 20 min, it can be seen from Figure S2b (Supporting Information) that the Al2p peak tends to shift again toward the higher binding energy value. While it is known that prolonged application of DUV in the presence of ozone atmosphere caters to the metal-oxide network formation, here we observe an optimum exposure condition of 20 min for the DUV lamp at a low intensity of 18 mW cm^{-2}.[19] Beyond this exposure duration, the un-quantified ozone release could result in the formation of unstable oxygen radicals thereby reacting with the surface. The unstable oxygen radical assists the hydroxide formation before the metal oxide network, thereby requiring an increased amount of DUV exposure.[20] Further, high-resolution O1s spectra for DUV-exposed and Th-annealed samples for the different times are shown in **Figure** 2a,b, respectively.

The O1s peak observed for the soft bake sample is also shown in Figure S3 (Supporting Information). The two most significant peaks obtained by deconvolution peak fitting in the O1s XPS

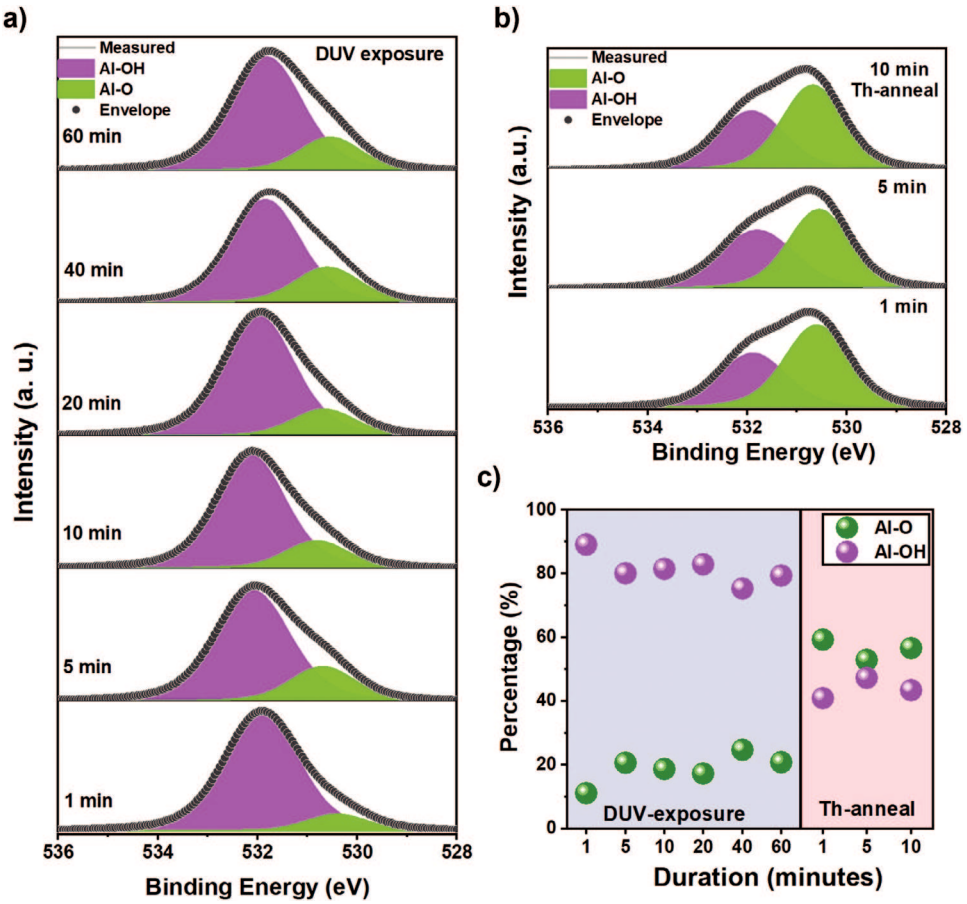

Figure 2. XPS spectra of O1s peaks for AlO_x thin films at different a) DUV-exposure and b) thermal-anneal duration. c) The calculated Al—O and Al—OH peak percentages from the peak fit analysis. The Al—O and Al—OH peaks were at 530.5 ± 0.3 and 532.2 ± 0.3 eV respectively.

spectra were attributed to the Al—O and Al—OH bonds at binding energies of 530.5 ± 0.3 and 532.2 ± 0.3 eV, respectively.[4,5] A greater area fraction of the Al—OH peak is known to be caused by the electrically active oxygen vacancies in the thin film,[5,18] whereas a high content of Al—O signifies an improved metal oxide network formation. It is evident that with a longer treatment time, the Al—O bonding increased due to the decomposition of the metal precursor. Simultaneously, the Al—OH percentage decreases as these bonds dissociate to form the Al—O bonds with increased exposure. Figure 2c shows the percentage contribution of Al—O and Al—OH bonds at different times indicating a possible saturation of the reactive effect of the applied annealing technique. As the two-peak deconvolution does not quantify the oxygen vacancy contribution clearly, we additionally performed a three-peak convolution of the O1s spectra as shown in Figures S4 and S5 (Supporting Information) (soft-bake sample). Herein, the Al—O, O^{2-}, and Al—OH peaks were attributed to the binding energy values of 530.5 ± 0.3, 531.5 ± 0.3, and 532.4 ± 0.3 eV, respectively with reference from earlier reports for similar metal oxides.[3,4,21,35] From this fitting, we observe that the optimum condition for the metal oxide formation using DUV exposure is 20 min, beyond which negligible change in the Al—O and O^{2-}contribution was observed. Additionally, the Th-anneal condition of 5 min showed the optimum Al—O concentration well in agreement with rapid thermal annealing conditions reported in the literature.[4] Finally, the peak percentage contribution from the Al2p and O1s spectra has been tabulated in Table S2 (Supporting Information), which concludes that the samples that underwent a Th-annealing for 5 min and DUV-exposure for 20 min, respectively, resulted in the optimum Al—O contribution for the metal oxide network formation.

Further, we examined the impact of the Th-annealing and DUV-exposure techniques on the oxide film roughness and thickness. **Figure 3**a,b shows the atomic force microscopy (AFM) images and the root-mean-square (σ_{RMS}) roughness of the optimized Th-annealing and DUV-exposure settings of 5- and 20-min respectively. It was observed that the DUV-exposed sample had a low σ_{RMS} of 89.4 pm over 423.3 pm of the Th-annealed samples, indicating that the DUV-exposed samples are ultra-smooth and similar to the conventional silicon oxide wafer roughness.[36] Additionally, the cross-sectional transmission electron microscopy (TEM) measurements shown in Figure 3c,d for Th-annealed (5 min) and DUV-exposed (20 min) samples respectively show that both the annealing techniques deliver similar amorphous and dense AlO_x layer with a thickness of 3.46 and 3.79 nm. In addition, an interlayer of amorphous aluminum silicate ($AlSiO_x$) was also detected. This interlayer composition was confirmed by energy dispersive X-ray spectroscopy (EDS) measurements as

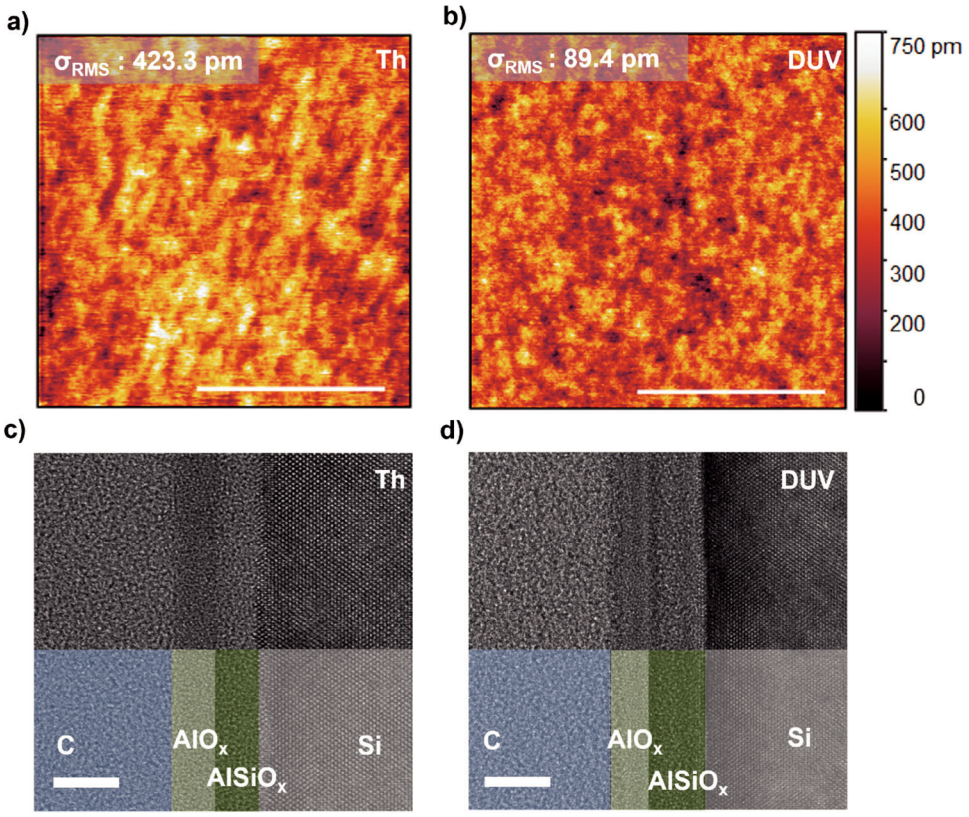

Figure 3. AFM and TEM images showing the surface morphology and thickness of as fabricated AlO_x films via a), c) thermal annealing and b), d) DUV exposure respectively. The scale bar in the AFM and TEM images correspond to 500 and 5 nm respectively. The EDS mapping for the TEM samples is included in Figure S6 (Supporting Information).

shown in Figure S6 (Supporting Information). The interlayer is observed due to the presence of a thin native oxide in the silicon samples.[23] The amorphous interlayer was observed to be thicker in the DUV-exposed (4 nm) over the Th-annealed (3.5 nm) films. $AlSiO_x$ interlayer formation can be attributed to the available reactive —OH radicals in the films which result in the Al—O—Si densification due to the oxygen-rich environment.[8,22,23]

2.3. Capacitors with Ultra-thin, Solution Sheared AlO_x

Post morphological and structural characterizations, electrical measurements were performed on the Th-annealed (300 °C for 5 min) and DUV-exposed films (1, 5, 10, and 20 min). Areal capacitance-frequency (*C–f*) and quasi-static capacitance-voltage (*C–V*) plots are shown in **Figure** 4a,b, respectively. Here, it is evident that the Th-annealed films clearly outperform the DUV-exposed samples, showing a capacitance value of 784 to 730 nF cm^{-2} between 20 and 10^5 Hz. The average capacitance value was 750 nF cm^{-2} which is by far, the best-reported capacitance value for an AlO_x thin film. With reference to previous reports, the optimized thermal annealing condition used in this research resulted in higher stability of the capacitance over the frequency sweep.[1,4] From the *C–f* measurements in Figure 4a, it is further observed that while there is an increase in the average capacitance value from 520 nF cm^{-2} to 580 nF cm^{-2} between the 1 and 10 min DUV-exposed films, the measurement on 20-min exposed DUV samples indicate a capacitance per unit area of 600 nF cm^{-2}. It should be noted that the above values are taken as an average capacitance throughout the frequency measurement range. Additionally, it is observed that the *C–V* plots show a very slight increase in capacitance with the applied bias voltage. Here, we attribute this increase to the utilization of n+Si as a bottom contact in our devices.[3] We specifically address the DUV exposure and its potential as a substitute for the relatively high-temperature Th (300 °C for 5 min) annealing. We discuss the AlO_x samples subjected to different exposure durations to evaluate their feasibility.[37] For reference, the capacitance obtained for the soft bake condition is also mentioned in Figure S7 (Supporting Information).

The capacitance values extracted from *C–f* and *C–V* measurements are shown for the different methods and annealing times in Figure 4c, where each data point represents the average of five devices measured at the respective condition. It is evident from this plot that while there is a linear increase in the capacitance value between the 1 and 10 min DUV-exposed films, the measurement on 20 min exposed DUV sample indicated a saturation in the areal capacitance. We avoid the overestimation of these capacitance values by plotting the average and deviation for the samples within the frequency range of 10–100 kHz. It should be noted that these measurements include the $AlSiO_x$ interlayer as discussed earlier from TEM measurements.

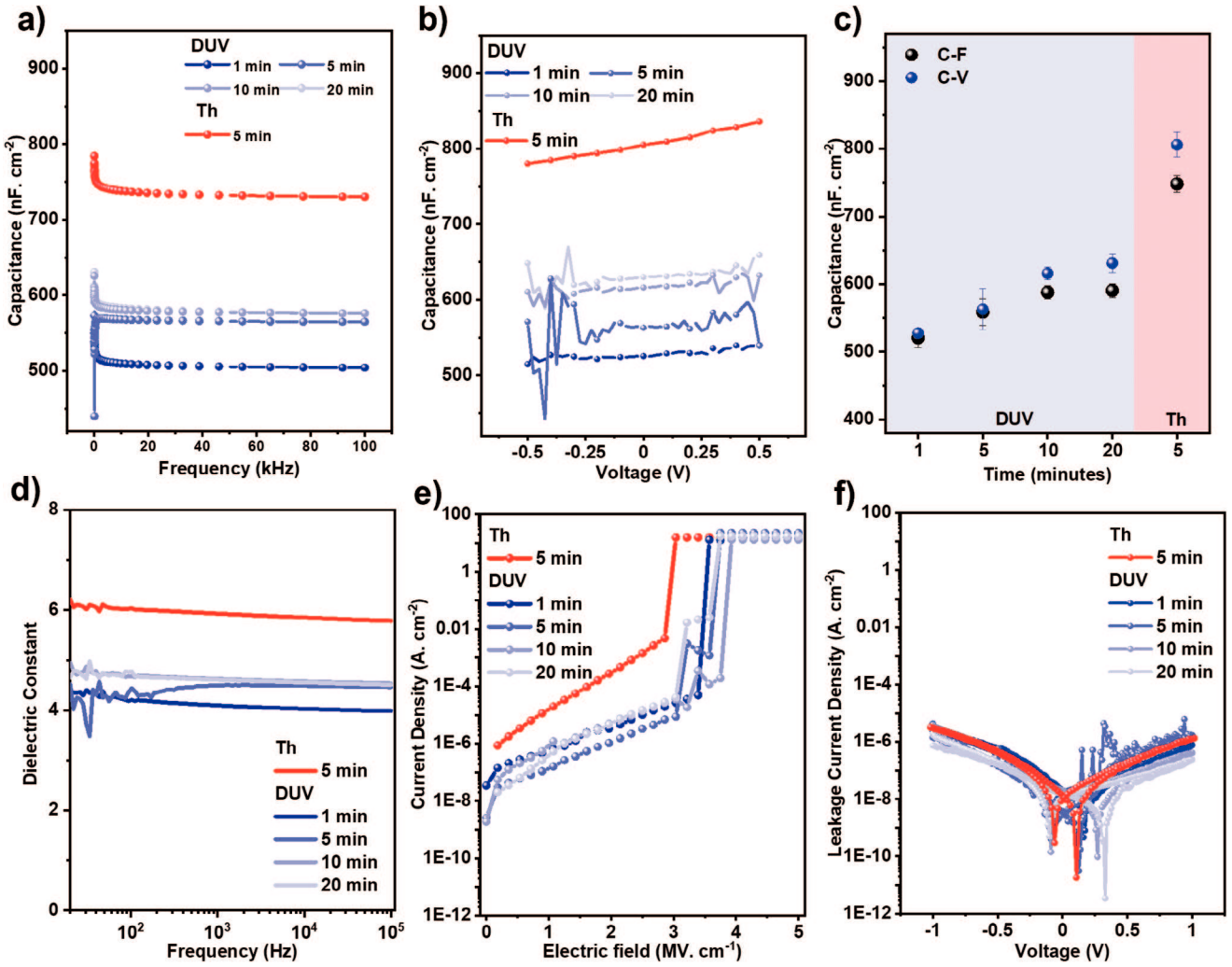

Figure 4. Single layer AlO_x a) capacitance-frequency (*C–f*) and b) quasistatic capacitance-voltage (*C–V*) measurements followed by c) corresponding average area-normalized capacitance calculated from a) (between 10 and 100 kHz) and b). d) Dielectric constant values calculated with data from *C–f* measurements. e) The breakdown field and f) leakage current density. The red and blue colors correspond to thermal annealing and DUV-exposure annealing, respectively.

Interestingly, while the overall films' physical qualities were similar, the Th-annealed samples showed higher capacitance values than the DUV-exposed samples. This is attributed to the Al—O percentage difference between the Th-annealed and DUV-exposed samples, with the latter owing to the higher density of oxygen vacancies resulting in thicker $AlSiO_x$ interlayers.[23] Additionally, the dielectric constant (ε) values were evaluated using the *C–f* and TEM thickness measurements as depicted in Figure 4d. Multiple reports suggest that the ε of solution-processed AlO_x thin film is in the range of 4–7.[1–3,13,19,24,38–40] Here, from TEM, we observe that the overall thickness for the samples stands at 7 nm which is a combination of AlO_x and $AlSiO_x$ layers. From calculations at 10 kHz, the Th-annealed sample had a ε of 5.9 while it was 4.0, 4.4, 4.5, and 4.5 for the 1, 5, 10, and 20 min DUV-exposed samples respectively. Overall, we observe a reduced ε value in DUV-exposed samples in comparison to Th-annealed samples due to the higher $AlSiO_x$ thickness as depicted in Figure 3. Additionally, ε is possibly decreased due to the higher Al—OH content as illustrated in Figure 2. Together, due to higher $AlSiO_x$ thickness and Al—OH content, the ε value of the DUV-exposed films were in the range of 4.0–4.5, increasing relative to the DUV exposure time.

Finally, the current density for the electric field applied to the respective samples is shown in Figure 4e. It is found that at 1 MV cm^{-1}, the current density is roughly two orders of magnitude lower in the DUV-exposed samples than in the Th-annealed AlO_x thin films. The DUV-exposed samples were stable up to an electric field strength of 3 MV cm^{-1} whereas the Th-annealed samples exhibited a breakdown at 2.7 MV cm^{-1}. Additionally, a minor step-like increase in the current density in DUV-exposed samples suggested a potential $AlSiO_x$ interlayer breakdown, followed by the actual breakdown post 3.5 MV cm^{-1} as shown in Figure S8 (Supporting Information). In Figure 4f, the leakage current density (*J–V*) in the range of 1 to 1 V further underscores the durability of DUV photo-activated dielectric films with a maximum at 10^{-7} A cm^{-2} in comparison to the Th-annealed film at

Table 1. Data of solution processed AlO_x thin films for electronic devices retrieved from literature.

Coating Technique	Solvent	Annealing method	Annealing conditions	Thickness [nm]	Capacitance [nF·cm^{-2}]	Leakage Current Density [A.cm^{-2}]	Breakdown [MV cm^{-1}]	Reference
Spin-coating	H_2O	Thermal	100 °C, 250 °C/5 min each/layer + 250 °C/2 h	100	47.7	10^{-5}	4	[38]
Spin-coating[a)]	H_2O	Thermal	300/60 min	60	133	–	–	[13]
Spin-coating	2-ME	UV (253 nm)	80 min, 65.5 mW·cm^{-2}	40	180	8×10^{-9}	3.5	[19]
Solution shearing	H_2O	Thermal	300 °C/1 min per layer	20	208	1.3×10^{-8}	–	[4]
Spin Coating	2-ME+ Acetyl acetone	Thermal	300 °C/1 min	20	336	1.2×10^{-7}	2.7	[1]
Spin Coating	H_2O	Thermal+ UV (40 min)	150 °C/2 h	17.5	414	10^{-5}	≈2	[3]
			250 °C/2 h	16	390	10^{-8}	≈3.5	
			350 °C/2 h	15	418	10^{-9}	≈5.5	
			450 °C/2 h	14.3	446	10^{-9} (at 1 MV·cm^{-1})	≈5.5	
Spin Coating	Ethanol	Thermal+ Plasma	250 °C/30 min+ 30 W/30 min	–	242	10^{-5}	–	[41]
Spin Coating	Ethanol	Thermal	100 °C	151	920	79.6	0.7	[18]
			130 °C	89	1110	3.1×10^{-2}	1	
			200 °C	56	241	5.7×10^{-4}	3	
			300 °C	52	194	6.4×10^{-5}	3	
			400 °C	51	170	1.0×10^{-6}	3	
			500 °C (30 min)	47	163	9.8×10^{-7} (at ≈3 MV.cm^{-1})	3	
Solution shearing	H_2O	Thermal DUV (185+254 nm)	300 °C/5 min 20 min	7 7	750 600 (at 10 KHz)	10^{-6} 10^{-7}	2.7 3	This work

[a)] In ammonia gas atmosphere, 2-ME refers to 2-methoxyethanol.

10^{-6} A cm^{-2} confirming that these thin films can be employed for low-voltage transistor applications.

To compare the dielectric layer performance metrics with existing literature, the data has been tabulated as shown in **Table 1**. From this, we observe that the capacitance values obtained for AlO_x here using DI- water, low-temperature annealing, and time duration using solution shearing outperforms other conventionally processed AlO_x thin films with the highest capacitance of 750 and 600 nF cm^{-2} for Th-annealed and DUV-exposed samples with a thickness of 7 nm. It is important to note that while there is a claim of achieving >1000 nF cm^{-2} shown in the comparison table, it is indeed not applicable as a dielectric film due to its high leakage, thickness, and roughness metrics.[18] Overall, we observe that the AlO_x films reported in this work have a comparably low thickness and higher capacitance values. Further, it represents a simple one-time coating process along with reduced annealing time. The applicability and stability of these ultra-thin dielectric films in transistors are discussed in the next section.

2.4. OFETs with Ultra-thin, Solution Sheared AlO_x Dielectrics

Having shown the promising characteristics of the ultra-thin solution-sheared films with high capacitance and low-leakage currents, we proceed to evaluate their performance in organic field-effect transistors. The structure of the devices is shown in **Figure 5b**. Vacuum-deposited 2,9-Didecyldinaphtho[2,3-b:2′,3′-f]thieno[3,2-b]thiophene (C10-DNTT) with the structure shown in Figure 5a is used as the organic semiconductor to fabricate devices in a bottom-gate, top-contact configuration with thermally-evaporated Au source and drain electrodes.

We selected C10-DNTT as an organic semiconductor material in devices with the AlO_x dielectrics since it exhibits a relatively low contact resistance with gold contacts[42] and shows high field effect mobility even when evaporated films are employed.[43]

2.4.1. Growth of Organic Semiconductor

First, we studied the impact of the different annealing methods used for the preparation of the underlying AlO_x layer on the growth of the organic semiconductor. Since one of the annealing methods involves DUV exposure, the surface energy of both sub-

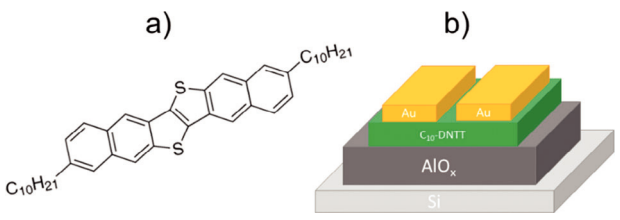

Figure 5. a) Structure of C10-DNTT semiconducting small molecule. b) Device structure of organic thin film transistor with ultra-thin, solution sheared AlO_x dielectric.

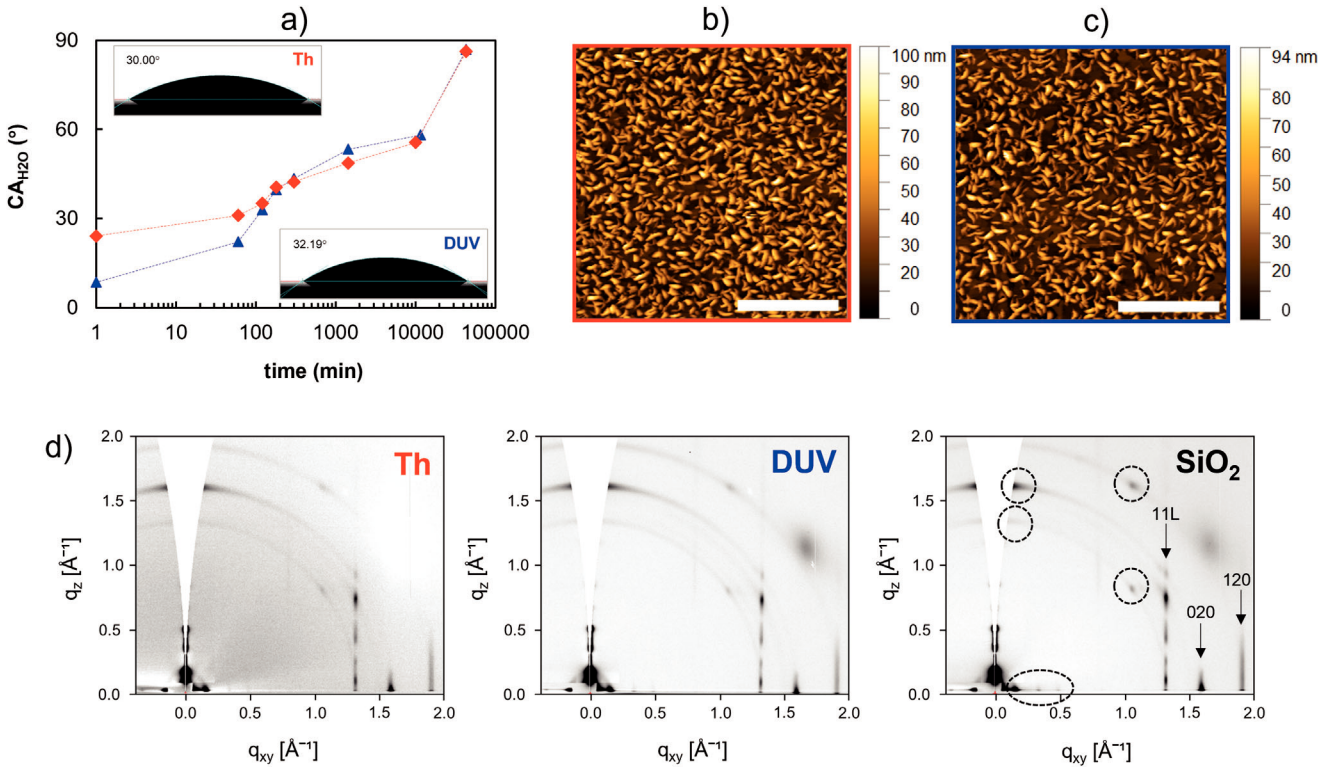

Figure 6. a) Change of water contact angle with time on DUV-exposed (blue symbols) and thermally annealed (red symbols) AlO_x; the inset shows the drop images after vacuum; b) AFM image of C10-DNTT grown on thermally annealed AlO_x; c) AFM image of C10-DNTT grown on DUV-exposed AlO_x. (AFM scale bars: 1 µm); d) 2D diffraction images of C10-DNTT on different dielectrics: thermally annealed AlO_x (left), DUV-exposed AlO_x (middle), and SiO_2 (right). The dashed markers indicate peaks originating from standing crystals.

strates is expected to differ substantially- at least for a short time after annealing. As the growth of the organic semiconductor is known to strongly depend on the substrate surface properties, we first studied the evolution of the water contact angle with time. **Figure** 6a shows how the contact angle changes after thin film preparation. Corresponding drop images are shown in Figures S9 and S10 (Supporting Information). It can be observed that the water contact angle on thermally annealed AlO_x is almost three times the value of the one obtained on DUV-exposed AlO_x. However, within a few hours after fabrication, both the values increase and start to converge. Furthermore, when examining the surface morphology of the semiconductor when grown onto the differently annealed AlO_x dielectrics, no major difference is seen. As shown by the AFM topography images in Figure 6b,c, C10-DNTT layers on both AlO_x films exhibit the commonly observed growth of vertical crystallites on top of a C10-DNTT base film as it is usually seen for vacuum-deposited films of this semiconducting material,[44,45] and which was also observed in our reference samples on Si with native and 300 nm silicon oxide (Figure S11, Supporting Information). Besides their similarity, films on DUV-exposed substrates show slightly less coverage with these vertical crystallites.

In Figure 6d we show 2D diffraction images obtained from grazing-incidence wide-angle X-ray scattering (GIWAXS) measurements of C10-DNTT grown on thermally annealed and DUV-exposed AlO_x as well as on SiO_2, which served as a reference substrate in this study. The GIWAXS diffraction images show the characteristic Bragg rods from the base films in the in-plane direction indicating its high crystallinity and well-aligned molecules with respect to the AlO_x surfaces. Furthermore, the typical signature of the standing crystallites (group of lying down molecules[45]) is observed (indicated with dashed markers). Comparing the images of DUV- and Th annealed samples, no major difference with respect to the in-plane peak positions or full width at half maximum (indicating crystallite size) can be observed (see Table S3, Supporting Information). However, it might be worth mentioning that the in-plane peaks of C10-DNTT on UV-annealed AlO_x move to slightly higher q-values. Hence, with the distances reduced, one might expect improved charge transport in those devices (for values see Table S3, Supporting Information).

The absence of considerable morphological differences in the C10-DNTT films appears difficult to reconcile with the different contact angles that were measured for the differently produced dielectric layers right after fabrication. However, this finding could be explained if the contact angles of the differently produced AlO_x surfaces significantly changed from their initial values during the window of time between the end of dielectric layer fabrication and the beginning of the organic semiconductor deposition in the high vacuum evaporation chamber. To test this hypothesis, we measured the contact angles after subjecting the AlO_x substrates to high vacuum conditions similar to those used for the deposition of the organic semiconductor. The inset in Figure 6a shows the drop images used for this

contact angle measurement. It can be seen that in a vacuum (more precisely during the time it takes to reach a high vacuum from ambient pressure), the contact angles change and converge to approximately the same value for both DUV and thermally annealed dielectric layers. Thus, the surface polarity would be similar for both dielectric layer versions at the time the semiconductor is deposited. Hence, we conclude that the annealing protocol has only a very minor impact on the growth of the organic semiconductor and C10-DNTT films on both types of AlO_x dielectric resembling the ones on Si and SiO_2 substrates.

The evolution of C10-DNTT morphology on the DUV and thermally annealed AlO_x thin films showed a similar variation with a change in storage time of the prepared films (thereby contact angle) as shown in the AFM images in Figure S12 (Supporting Information). It was observed that irrespective of the annealing condition employed for the formation of AlO_x films, the morphology on "long time stored" (>1 month) samples appears rather different to the as-prepared AlO_x films – with larger standing crystals that seem to be ordered and less dense on the base layer. This difference concerning the surface polarity is corroborated by the GIWAXS diffraction images through the strongly reduced intensity/disappearance of the rings (Figure S13, Supporting Information). Importantly, the comparison between Th-annealed and DUV-exposed films is consistent, independent of the point in time of semiconductor deposition. This observation is likely related to the higher dielectric constant of Th-annealed films, which is commonly associated with the increased polar dielectric surface disorder thus leading to reduced field effect mobilities.[46–48]

Moreover, as it is common to treat the dielectric with self-assembled monolayers (SAMs), small differences in the untreated dielectric's surface energetics as reported here are not likely to be technologically relevant. As part of substrate cleaning or surface activation prior SAM deposition it is very common to expose the substrate to a UV/ozone treatment. To emulate this situation, we grew C10-DNTT on thermally annealed and DUV-exposed AlO_x with an extra UV/ozone–treatment. Figure S12 (Supporting Information) shows the morphologies of the resulting C10-DNTT layers. Similar morphologies are observed on dielectrics prepared with thermally and DUV-exposed substrates, which further supports our conclusion that there is only a minor effect of the fabrication process (DUV-exposed versus Th-annealed) on the growth of the organic semiconductor.

2.4.2. Comparison of OFETs with DUV-exposed and Thermally-Annealed AlO_x

Based on our previous findings, for the comparison of transistors with DUV- and Th annealed AlO_x dielectrics, we ensured the use of substrates that were prepared at the same time. The semiconductor was deposited within 24 h of the fabrication, yielding morphologies comparable to the ones in Figure 6. **Figure 7** shows transfer and example output curves of representative devices with DUV-exposed and Th-annealed dielectric. We further show the device mobility as a function of V_{gs} for a representative device in Figure 7c and the distribution of the subthreshold swing in Figure 7d. The distribution of the threshold voltage is also shown in Figure S14a (Supporting Information). We note that the latter is slightly affected by variations that are introduced by the unavoidable illumination of devices during the contacting of the OFETs (see Figure S14b, Supporting Information). As can be seen in Figure S14b (Supporting Information), the threshold voltage of devices slowly shifts to more positive voltages with increased duration of illumination by the microscope lamp. This effect, which appears to be slightly higher for DUV-exposed samples (see Figure S14c,d, Supporting Information), is also seen for reference devices on SiO_2 (see Figure S15, Supporting Information). Hence, we attribute the slightly increased V_{th} variation to the effect of light. The subthreshold swing of devices with DUV-exposed dielectric was on average better than the ones with Th annealed dielectric. The average subthreshold swing of DUV-exposed dielectric OFETs was 116 ± 22 mV dec^{-1} with a minimum value of 82 mV dec^{-1}. The lowest subthreshold swing of devices with thermally annealed dielectric was 99 mV dec^{-1} and the average was 139 ± 28 mV dec^{-1}. We attribute the better subthreshold swing of DUV-exposed devices to the lower surface roughness of these films and a resulting slightly lower density of trap states at the semiconductor-dielectric interface. To ensure that this conclusion is not affected by the microscope light illumination, we also intentionally shifted the transfer curves to different turn-on voltages by applying either light or slightly increased voltage. The result is shown in Figure S16 (Supporting Information). It can be seen that despite the large differences in V_{th}, the subthreshold swing and device mobility appear to remain relatively constant for both – devices with DUV- and thermally annealed AlO_x. The average mobility of OFETs with thermally annealed dielectrics was 1.30 ± 0.24 cm^2 V^{-1} s^{-1}. On the DUV-exposed dielectric, an average mobility of 3.3 ± 0.53 cm^2 V^{-1} s^{-1} was achieved. The higher average mobility of DUV-exposed devices can also be attributed to the better semiconductor-dielectric interface with a reduced density of shallow traps.

To see the impact of morphology and confirm the above results, we further fabricated devices on long-time stored (>1 month, yielding very high, water contact angles of ≈90°) AlO_x films. The capacitance values for these "aged" AlO_x samples were also evaluated as shown in Figure S17 (Supporting Information). It is important to note that the capacitance values of 745.99 and 580.17 nF cm^{-2} obtained from these measurements were used to evaluate the electrical parameters of the OFETs prepared on these "aged" AlO_x films. Representative transfer and output curves are shown in Figure S18 (Supporting Information). It is noted that devices prepared on "aged" AlO_x have generally even improved characteristics with the differences observed between OFETs with DUV-exposed and Th-annealed AlO_x being similar to the devices discussed above (Figure 7). The mobility of OFETs with DUV-exposed AlO_x was on average 6.1 ± 0.9 cm^2 V^{-1} s^{-1}. The threshold voltage was shifted closer to zero Volt (−0.14 ± 0.07 V) and the subthreshold swing was ≈96 ± 16 mV dec^{-1}, which is on average 20 mV dec^{-1} lower than for devices on "fresh" AlO_x films. As for the devices with Th annealed AlO_x, as previously, lower average mobility values of ≈2.8 ± 0.14 cm^2 V^{-1} s^{-1} were determined. Also, for devices with "aged" thermally annealed films, V_{th} shifted closer to zero (−0.06 ± 0.01 V). The average subthreshold swing of these devices was 115 ± 6 mV dec^{-1}, which is higher than for DUV-exposed devices, but on average 24 mV dec^{-1} lower than on the as-fabricated thermally annealed AlO_x surfaces. These findings highlight that the performance of devices with ultra-thin

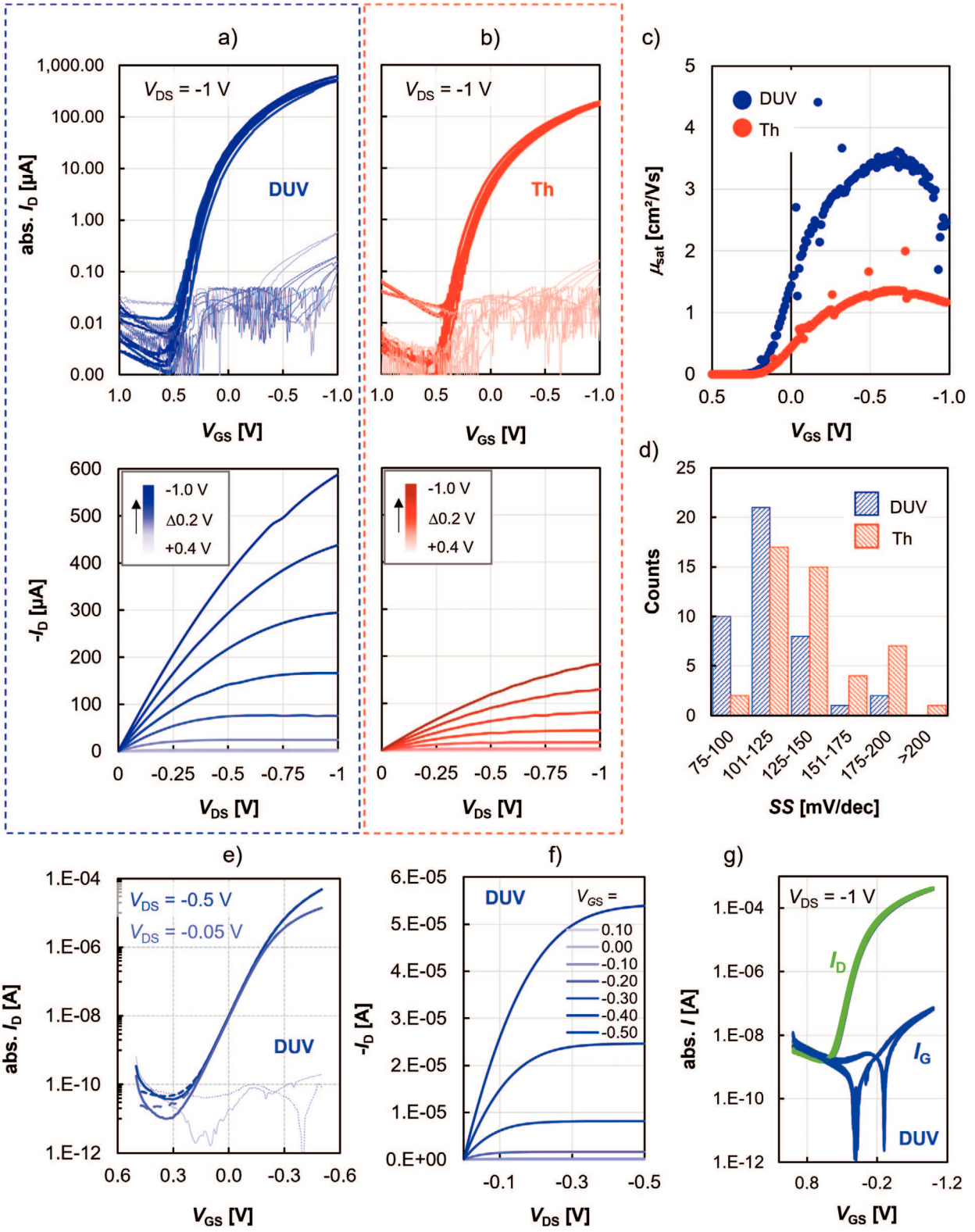

Figure 7. Comparison of OFETs using DUV-exposed (20 min) and thermally annealed (300 °C, 5 min) AlO_x. a) Transfer characteristics and representative output curves of DUV-exposed OFETs, b) transfer characteristics and representative output curves of thermally annealed OFETs, c) representative µ (V_{gs}) plots of OFETs with thermally and DUV-exposed AlO_x, d) distribution of subthreshold swing; e) transfer curve of an OFET with DUV-exposed dielectric operated at only 500 mV maximum bias, f) output curves of an OFET with DUV-exposed dielectric operated at max. 500 mV, g) stability of an OFET with DUV-exposed dielectric during repeated cycling (100 times).

Table 2. Literature values for OFETs with solution-processed gate dielectrics or AlO_x dielectric and vacuum-deposited C10-DNTT semiconducting layer.

Dielectric	preparation	bias/V_G/sat. [V]	V_{th} [V]	Mobility [$cm^2 V^{-1} s^{-1}$]	SS [mV dec^{-1}]	Reference
AlO_x	Spin-coating	−3	−0.72	1.8	110	[19]
Novel Polymers						[49]
−MBHSt	Spin-coating	−20	−2.61	0.25	677	
−FMBHSt			−5.05	0.76	582	
−MBHCa			−1.44	0.28	752	
−FMBHCa			−4.26	1.18	548	
Novel Polymers						[50]
−MBHCa-F-0.4	Spin-coating	−20	−1.45	0.14	258	
−MBHCa-F-0.1			−1.10	0.12	327	
−MBHCa-F-0.0.06			−0.58	0.07	332	
−MBHCa-F-0.01			−0.82	0.02	330	
SiO_2/AlO_x	Thermal growth/ALD	−40	–	8[a),b)]	–	[43]
AlO_x (3.6 nm)	Plasma oxidation	−3	−0.67	4.43 [a),b),c)]	89	[51]
Novel high-k polymer	Spin-coating	−10	−3.46	1.02	600	[52]
PAA	Spin-coating	−20	−1.56	4.29	na	[53]
PVA-based	EHD printing	−20	−3.12	0.915	776	[54]
AlO_x	Solution-shearing	−1	−0.14	6.1	96	This work

[a)] Substrate holder was heated during deposition; [b)] AlO_x coated with phosphonic acid (TDPA); [c)] TDPA thickness: 1.7 nm.

AlO_x dielectrics can be even further enhanced through the optimization of the OSC-dielectric interface for OFETs.

From the above discussions, we conclude that C10-DNTT-based transistors with DUV-exposed dielectrics generally have higher mobility and a steeper subthreshold slope than the devices with Th-annealed dielectric films. Moreover, also with the solution sheared polymer semiconductor Poly[2,5-bis(2-octyldodecyl) pyrrolo[3,4-c]pyrrole-1,4(2H,5H)-dione −3,6-diyl)-alt-(2,2′;5′,2″;5″,2‴-quaterthiophen-5,5‴-diyl)] (PDPP4T) higher performance is observed for devices with DUV-exposed AlO_x layer as compared to the ones based on the Th annealed dielectric (Figure S19, Supporting Information). Hence, we can state that while excellent devices can be achieved on both the Th and DUV annealed dielectrics, DUV-annealing is a promising alternative to high-temperature thermal annealing of AlO_x thin films and can facilitate device characteristics that outperform the ones based on the thermal approach.

To highlight the utility of DUV-exposed AlO_x films for OFETs, further measurements were conducted. The low subthreshold swing, threshold voltage that can be tuned to values close to zero, and high mobility further allow for the operation of the devices at even lower voltage, which is shown in Figure 7e,f. The device with a subthreshold swing of 93 mV dec^{-1} operates at only ± 500 mV gate voltage with a reasonably good I_{on}/I_{off} of 3.7×10^5. From Figure 7g, it can be further seen that devices with ultra-thin, solution-sheared, and DUV-exposed dielectric exhibit excellent stability during repeated cycling between the on- and off-state. Specifically, we find only a minor V_{th} shift of 40 mV when the device is cycled 100 times. The V_{th} shift to slightly more positive voltages (from 110 to 150 mV) might be related to the measurement environment not being completely dark. A zoomed-in view and the fitted V_{th} can be found in Figure S20 (Supporting Information).

In the future, the subthreshold swing might be further enhanced through the employment of dielectric surface treatments such as phosphonic acids and the use of highly crystalline solution-coated semiconductor layers, which can effectively reduce trap density. For now, we conclude that DUV-exposed, low-temperature processed, ultra-thin gate dielectrics prepared from water-based precursor solutions are a promising route toward the fabrication of electronics with distinctly reduced environmental impact while being very competitive from a device perspective.

In **Table 2**, we compare the fabricated OFETs to other reported devices that utilize vacuum-deposited C10-DNTT but different solution-fabricated gate dielectrics or AlO_x prepared by various means.

First, one can see that most of the literature-reported devices operate distinctly above ±1 V. Furthermore, the most similar sample with spin-coated AlO_x[19] has comparably lower mobility and higher SS than the best devices obtained in our study. The devices with comparable AlO_x thickness but prepared by plasma oxidation have rather similar characteristics.[51] Yet, the interface with the organic has been modified with tetradecylphosphonic acid (TDPA), and sample heating during thermal sublimation of the semiconductor has facilitated the growth of larger crystallites, a potential that we have not explored with our dielectric layers yet.

3. Conclusion

In summary, we have shown the utilization of DI- water-based precursor solutions for ultra-thin AlO_x dielectric films fabricated by solution shearing. Thermal annealing and DUV exposure were employed and compared to evaluate the suitability of the AlO_x films as dielectric layers. By studying the *C–f* and *C–V* behavior, breakdown voltage, and leakage current density of these samples we confirmed that the Th-annealed samples had

a higher areal capacitance of 750 nF cm^{-2}, in comparison to the DUV-exposed samples with 600 nF cm^{-2}. Additionally, the DUV annealed samples showed very promising electrical and morphological properties with a leakage current density of $2 \cdot 10^{-7}$ A cm^{-2} at 1 MV cm^{-1} and a surface roughness similar to that of silicon oxide (89.4 pm) superior to the Th annealed samples.

These dielectrics then were used in OFETs with C10-DNTT as a semiconductor wherein the devices with DUV-exposed dielectrics achieved a higher average mobility of 6.1 cm^2 V^{-1} s^{-1}, near-zero threshold voltage and a steeper subthreshold slope of 96 mV dec^{-1} than the devices with Th-annealed dielectric films. Finally, devices with the solution-sheared polymer semiconductor, PDPP4T with DUV-exposed AlO_x layer were shown to follow the C10-DNTT device metrics with enhanced device characteristics as compared to the ones based on the Th annealed dielectric. With this, the environmental impact regarding emissions, energy demand, resource depletion, and toxicology can be reduced for such processes.

4. Experimental Section

Preparation of Precursor Solution:: A 0.2 mol L^{-1} solution of Aluminum nitrate nonahydrate [Al $(NO_3)_3.9H_2O$ 99.997% trace metals basis, Sigma Aldrich] in DI-water was prepared and stirred at RT for 1 h. The solution was then filtered through a 0.2 µm PTFE syringe filter before being used for coating.

Thin Film Preparation: Heavily doped silicon (Si) wafers were used as substrates for the devices. Prior to use, all the substrates went through a cleaning cycle for 15 min each of DI water, acetone, and isopropanol in an ultrasonication bath. Post-sonication, the substrates were dried using N_2. The substrates were then activated in a DUV-ozone chamber for 10 min.

All AlO_x films were prepared by solution shearing with a custom-built laboratory setup. During coating, the blade angle was set at 8° with a gap of 50 µm between the edge of the blade and the substrate. 2.5 µL of precursor solution for 1.5 inch × 0.5-inch Si substrate was injected at the interface between the substrate and the blade. During coating, the substrate temperature was set to 80 °C, and the coating speed was 10 mm s^{-1}. Thermally annealed samples (denoted as "Th") were baked on a hot plate at 300 °C for 5 min. For DUV- exposure (samples named "DUV"), the as-coated films were transferred to a UV lamp-installed chamber from Dinies Technologies GmbH with emission peaks at 185 (33%) and 254 nm (67%). Later, samples were annealed for 20 min post a soft bake of 120 °C for 2 min (if not otherwise stated). While care was taken to place an exhaust above the UV source to eliminate the presence of ozone atmosphere, it was believed that there was a possibility of ozone traces still being available for metal oxide network formation.

Thin Film Characterization: TEM measurements were conducted using a JEOL JEM F200 operated at 200 kV acceleration voltage equipped with a GATAN OneView CMOS camera for fast imaging. Local EDS analysis was performed using a dual 100 mm^2 window-less silicon drift detector.

XPS samples were transferred to an ultrahigh vacuum chamber (ESCALAB 250Xi by Thermo Scientific, base pressure: 2×10^{-10} mbar). The measurements were carried out using an XR6 monochromated Al Kα source ($h\nu$ = 1486.6 eV) and a pass energy of 20 eV. The spectra were normalized, and calibrated according to C1s peak at 284.8 eV. The data was analyzed using the Avantage software from Thermo Scientific.

AFM images were obtained with a Nanosurf FlexAFM in tapping mode at a 70% setpoint, 300 mV vibration amplitude, and a vibration frequency of 159.52 kHz. The images were analyzed using Gwyddion 2.59 data visualization and analysis tool. TAP-190Al-G cantilever tips with a resonance frequency of 190 kHz from Budget Sensors were used for the measurements.

Water contact angles were measured with a Data Physics OCA series goniometer.

Grazing-incidence wide-angle X-ray scattering (GIWAXS) measurements were performed at beamline P08 at the German Electron Synchrotron (Deutsches Elektronen-Synchrotron) DESY, Hamburg, Germany. The energy of the beam was 18 keV and the dimensions of the beam were 100 µm (vertically) and 400 µm (horizontally). The images were recorded using a Perkin Elmer 1620 area detector which was placed 707 mm behind the sample. The sample-to-detector distance and position of the beam on the detector were verified using a lanthanum hexaboride calibration standard. The incidence angle of the beam was 0.07° and the samples were exposed for 30 s. Data correction, background subtraction, and analysis were performed using WxDiff software.

Devices Fabrication and Measurement: For OFET preparation, the organic semiconductor (C10-DNTT) was vacuum-deposited with a rate of 0.2 As^{-1} to an approximate thickness of 25 nm. The polymer devices (PDPP4T) were prepared by solution shearing at room temperature from a 12 mg ml^{-1} solution in chloroform. The shearing speed was 2 mm s^{-1}. Device fabrication was finished by thermal evaporation of Au top source and drain electrodes with a thickness of 50 nm at a rate of 1.5 A s^{-1}.

For capacitance measurements, Al electrodes with thickness of 50 nm were deposited by thermal evaporation using shadow masks under a very high vacuum of 10^{-7} mbar with a deposition velocity of 1.5 Å s^{-1}.

The coating, annealing, and morphology measurements were performed in the ambient atmosphere with a relative humidity of ≈30%.

C–V and measurements were done on a Keysight B1500 Semiconductor Analyzer with a 25-mV step and a 1 s delay in the measurements. *C–f* measurements were performed using a Keysight E4980A Precision LCR meter run by the SweepMe! software. OFET measurements were done utilizing a Keithley 4200A-SCS Parameter Analyzer in a dark room at ambient conditions. The effective field-effect mobility of devices in saturation was calculated using the equation $\mu_{eff} = \frac{2L}{WC_i} \left(\frac{\partial \sqrt{|I_{DS}|}}{\partial V_{GS}}\right)^2$ from the fitted linear slopes between V_{th} and maximum V_{GS}. Here, C_i was the capacitance per unit area of the dielectric, W was the channel width, and L was the channel length. The V_{TH} was obtained from the intercept of the linear fit of the $I_{DS}{}^{1/2}$ versus V_G curve and the x-axis. In this report, the channel width and length for all devices were 18 230 and 50 µm respectively unless otherwise specified. For calculation the capacitance values obtained from capacitor characterization (DUV-exposed: 600 nF cm^{-2}, Th-annealed: 750 nF cm^{-2}) were used. Further capacitance values for the "aged" samples on which OFETs were measured had capacitance values of 580.17 and 745.99 nF cm^{-2} respectively for the DUV-exposed and Th-annealed samples.

Supporting Information

Supporting Information is available from the Wiley Online Library or from the author.

Acknowledgements

The authors acknowledge DESY (Hamburg, Germany), a member of the Helmholtz Association HGF, for the provision of experimental facilities. Parts of this research were carried out at PETRA III and authors would also like to thank Dr. Chen Shen for assistance in using beamline P08. Beamtime was allocated for proposal I-20230095. The authors acknowledge Shaoling Bai and Jonathan Perez Andrade for their support in carrying out the GIWAXS measurements. The authors also acknowledge the valuable inputs received from Tianyu Tang during the discussions. K.H. acknowledges the financial support by the TU Dresden and the Professorinnenprogramm III des Bundes und der Länder. This project received funding from the European Research Council (ERC) under the European Union's Horizon 2020 research and innovation program (ERC Grant Agreement no 714067, ENERGYMAPS).

Open access funding enabled and organized by Projekt DEAL.

Conflict of Interest

The authors declare no conflict of interest.

Author Contributions

P.D. and K.H. contributed equally to the work, designed the experiments, and fabricated all the samples. S.M. conceptualized the research along with P.D., K.H., and M.H. A.W. L. performed the XPS measurements and was assisted by Y.V. in the analysis of the data. V.M. helped with the fabrication and participated in the discussion of the results. M.H. performed GIWAXS measurements and K.H. analysed the data. D.P., A.T., and B.R. performed the TEM characterization. All authors approved the final version of the manuscript.

Data Availability Statement

The data that support the findings of this study are available from the corresponding author upon reasonable request.

Keywords

AlO_x, eco-friendly, high capacitance, metal oxide dielectrics, organic field-effect transistors, solution shearing, ultra-thin films, water-based

Received: December 12, 2023
Revised: May 8, 2024
Published online: July 2, 2024

[1] X. Zhuang, S. Patel, C. Zhang, B. Wang, Y. Chen, H. Liu, V. P. Dravid, J. Yu, Y. Y. Hu, W. Huang, A. Facchetti, T. J. Marks, *J. Am. Chem. Soc.* **2020**, *142*, 12440.
[2] A. Liu, H. Zhu, H. Sun, Y. Xu, Y. Noh, *Adv. Mater.* **2018**, *30*, 1706364.
[3] A. Liu, G. Liu, H. Zhu, B. Shin, E. Fortunato, R. Martins, F. Shan, *RSC Adv.* **2015**, *5*, 86606.
[4] T. Tang, P. Dacha, K. Haase, J. Kreß, C. Hänisch, J. Perez, Y. Krupskaya, A. Tahn, D. Pohl, S. Schneider, F. Talnack, M. Hambsch, S. Reineke, Y. Vaynzof, S. C. B. Mannsfeld, *Adv. Funct. Mater.* **2023**, *33*, 2207966.
[5] S. K. Vishwanath, H. Woo, S. Jeon, *Nanotechnology* **2018**, *29*, 235202.
[6] L. A. Majewski, R. Schroeder, M. Grell, *Adv. Mater.* **2005**, *17*, 192.
[7] T. B. Daunis, J. M. H. Tran, J. W. P. Hsu, *ACS Appl. Mater. Interfaces* **2018**, *10*, 39435.
[8] Y. M. Park, A. Desai, A. Salleo, L. Jimison, *Chem. Mater.* **2013**, *25*, 2571.
[9] P. Ma, J. Sun, G. Liang, Y. Li, Q. Xin, Y. Li, A. Song, *Appl. Phys. Lett.* **2018**, *113*, 063501.
[10] Y. Diao, B. C. K. Tee, G. Giri, J. Xu, D. H. Kim, H. A. Becerril, R. M. Stoltenberg, T. H. Lee, G. Xue, S. C. B. Mannsfeld, Z. Bao, *Nat. Mater.* **2013**, *12*, 665.
[11] L. A. Majewski, R. Schroeder, M. Grell, *Adv. Funct. Mater.* **2005**, *15*, 1017.
[12] S. Sagar, N. Mohammadian, S. Park, L. A. Majewski, B. C. Das, *Nanotechnology* **2020**, *31*, 255705.
[13] Q. Liu, C. Zhao, I. Z. Mitrovic, W. Xu, L. Yang, C. Z. Zhao, *Adv. Electron. Mater.* **2020**, *6*, 2000072.
[14] E. Carlos, J. Deuermeier, R. Branquinho, C. Gaspar, R. Martins, A. Kiazadeh, E. Fortunato, *J. Mater. Chem. C* **2021**, *9*, 3911.
[15] Y. Pan, Y. Song, C. Zhang, Q. Zhu, J. Wu, *Comput Ind Eng* **2024**, *189*, 109934.
[16] J. Müller, T. S. Böscke, U. Schröder, S. Mueller, D. Bräuhaus, U. Böttger, L. Frey, T. Mikolajick, *Nano Lett.* **2012**, *12*, 4318.
[17] X. Zhuang, J. S. Kim, W. Huang, Y. Chen, G. Wang, J. Chen, Y. Yao, Z. Wang, F. Liu, J. Yu, Y. Cheng, Z. Yang, L. J. Lauhon, T. J. Marks, A. Facchetti, *Proc Natl Acad Sci U S A* **2023**, *120*, 2017.
[18] W. Xu, H. Wang, F. Xie, J. Chen, H. Cao, J. B. Xu, *ACS Appl. Mater. Interfaces* **2015**, *7*, 5803.
[19] Q. Mu, Z. Chen, S. Duan, X. Zhang, X. Ren, W. Hu, *Front. Mater.* **2020**, *7*, 570002.
[20] R. A. John, N. A. Chien, S. Shukla, N. Tiwari, C. Shi, N. G. Ing, N. Mathews, *Chem. Mater.* **2016**, *28*, 8305.
[21] E. Carlos, R. Branquinho, A. Kiazadeh, P. Barquinha, R. Martins, E. Fortunato, *ACS Appl. Mater. Interfaces* **2016**, *8*, 31100.
[22] Y. M. Park, J. Daniel, M. Heeney, A. Salleo, *Adv. Mater.* **2011**, *23*, 971.
[23] W. J. Lee, J. G. Choi, S. Sung, C. H. Kim, S. Na, Y. C. Joo, S. Park, M. H. Yoon, *ACS Appl. Mater. Interfaces* **2021**, *13*, 2820.
[24] R. Branquinho, D. Salgueiro, L. Santos, P. Barquinha, L. Pereira, R. Martins, E. Fortunato, *ACS Appl. Mater. Interfaces* **2014**, *6*, 19592.
[25] M. Geiger, M. Hagel, T. Reindl, J. Weis, R. T. Weitz, H. Solodenko, G. Schmitz, U. Zschieschang, H. Klauk, R. Acharya, *Sci. Rep.* **2021**, *11*, 6382.
[26] S. Müller, S. Kube, Organic Photovoltaics- Truly Green Energy : " Ultra – Low Carbon Footprint " 2020, WHITEPAPER March **2020**.
[27] A. Maalouf, T. Okoroafor, Z. Jehl, V. Babu, S. Resalati, *Renew Sustain Energy Rev* **2023**, *186*, 113652.
[28] T. C. Kuo, C. Kuo, L. Chen, *Resour Conserv Recycl* **2022**, *182*, 106289.
[29] C. Teixeira da Rocha, K. Haase, Y. Zheng, M. Löffler, M. Hambsch, S. C. B. Mannsfeld, *Adv. Electron. Mater.* **2018**, *4*, 1800141.
[30] K. Haase, M. Hambsch, C. Teixeira da Rocha, J. Zessin, S. C. B. Mannsfeld, in *Handbook of Organic Materials for Electronic and Photonic Devices*, Elsevier, Netherlands **2019**, 551.
[31] K. Umeda, T. Miyasako, A. Sugiyama, A. Tanaka, M. Suzuki, E. Tokumitsu, T. Shimoda, *J. Appl. Phys.* **2013**, *113*, 184509.
[32] F. Cordier, E. Ollivier, *Surf. Interface Anal.* **1995**, *23*, 601.
[33] "X-ray photoelectron spectroscopy of atomic elements," can be found under https://www.thermofisher.com/de/de/home/materials-science/learning-center/periodic-table.html (accessed: October 2023).
[34] C. D. Wagner, D. E. Passoja, H. F. Hillery, T. G. Kinisky, H. A. Six, W. T. Jansen, J. A. Taylor, *J. Vac. Sci. Technol.* **1982**, *21*, 933.
[35] J. T. Kloprogge, L. V. Duong, B. J. Wood, R. L. Frost, *J. Colloid Interface Sci.* **2006**, *296*, 572.
[36] X. Blasco, D. Hill, M. Porti, M. Nafría, X. Aymerich, *Nanotechnology* **2001**, *12*, 110.
[37] J. H. Park, S. J. Lee, T. Il Lee, J. H. Kim, C. H. Kim, G. S. Chae, M. H. Ham, H. K. Baik, J. M. Myoung, *J. Mater. Chem. C* **2013**, *1*, 1840.
[38] Y. S. Rim, H. Chen, T. B. Song, S. H. Bae, Y. Yang, *Chem. Mater.* **2015**, *27*, 5808.
[39] S. Gupta, S. Hannah, C. P. Watson, P. Šutta, R. H. Pedersen, N. Gadegaard, H. Gleskova, *Org. Electron.* **2015**, *21*, 132.
[40] M. S. Kang, W. J. Cho, *J. Phys. Chem. Solids* **2018**, *123*, 52.
[41] Q. H. Liu, C. Zhao, C. Z. Zhao, I. Z. Mitrovic, S. Hall, W. Y. Xu, L. Yang, E. G. Lim, Q. N. Wang, Y. L. Wei, Y. X. Cao, in 2019 Int. Conf. IC Des. Technol., IEEE, **2019**, pp. 1–5.
[42] J. W. Borchert, *On the Minimization of Contact Resistance in Organic Thin-Film Transistors*, Universität Stuttgart, Stuttgart, Germany **2020**.
[43] R. Hofmockel, U. Zschieschang, U. Kraft, R. Rödel, N. H. Hansen, M. Stolte, F. Würthner, K. Takimiya, K. Kern, J. Pflaum, H. Klauk, *Org. Electron.* **2013**, *14*, 3213.
[44] F. Talnack, S. Hutsch, M. Bretschneider, Y. Krupskaya, B. Büchner, M. Malfois, M. Hambsch, F. Ortmann, S. C. B. Mannsfeld, *Mol Syst Des Eng* **2022**, *7*, 507.
[45] B. Peng, X. Jiao, X. Ren, P. K. L. Chan, *ACS Appl. Electron. Mater.* **2021**, *3*, 752.
[46] J. Veres, S. Ogier, G. Lloyd, D. de Leeuw, *Chem. Mater.* **2004**, *16*, 4543.
[47] A. Köhler, H. Bässler, *Electronic Processes in Organic Semiconductors*, Wiley, Hoboken **2015**.
[48] H. Sirringhaus, *Adv. Mater.* **2005**, *17*, 2411.
[49] H. Kwon, H. Ye, K. Shim, H. G. Girma, X. Tang, B. Lim, Y. Kim, J. Lee, C. E. Park, S. Jung, J. M. Park, Y. J. Jung, D. Hwang, H. Kong, S. H. Kim, *Adv. Funct. Mater.* **2021**, *31*, 2007304.

[50] H. Ye, K. Y. Ryu, H. Kwon, H. Lee, R. Wang, J. Hong, H. H. Choi, S. Y. Nam, J. Lee, H. Kong, S. H. Kim, *ACS Appl. Mater. Interfaces* **2023**, *15*, 32610.
[51] U. Kraft, K. Takimiya, M. J. Kang, R. Rödel, F. Letzkus, J. N. Burghartz, E. Weber, H. Klauk, *Org. Electron.* **2016**, *35*, 33.
[52] T. Xu, Y. Liu, Y. Bu, S. Shu, S. Fan, M. Cao, T. Liu, J. Zou, J. Su, *Adv. Electron. Mater.* **2023**, *9*, 2200984.
[53] R. Wang, J. Lee, J. Hong, H. Kwon, H. Ye, J. Park, C. E. Park, J. H. Kim, H. H. Choi, K. Eom, S. H. Kim, *Polymers (Basel)* **2021**, *13*, 3715.
[54] C. Jung, X. Tang, H. Kwon, R. Wang, S. M. Oh, H. Ye, Y. R. Jeong, Y. J. Jeong, S. H. Kim, *Adv. Eng. Mater.* **2022**, *24*, 2100900.